UNDER PEER REVIEW

Original Research Article

Spectroscopic Investigation and Magnetic Study of Iron, Manganese, Copper and Cobalt-doped Hydroxyapatite Nanopowders

Abstract:

Pure, $Mn^{+2,}$ and Fe^{+3}- doped hydroxyapatite (HAp) nanoparticles were synthesized by the wet chemical method. Another two samples were prepared by mixing Mn^{+2} with Cu^{+2} into HAp (Mn-Cu HAp) and Fe^{+3} with Co^{+2} into HAp (Fe-Co HAp). All samples were prepared without change in the stoichiometric ratio of Ca/P inside the structure of HAp. Samples were characterized by different types of techniques such as XRD, FTIR, ESR, SEM and EDX. The measurements revealed that a typical HAp powder patterns were obtained. Comparing with pure HAp, Mn^{+2} substituted HAp (Mn-HAp) and Fe^{+3} substituted HAp (Fe-HAp) did not demonstrate significant structure deviation. Since the ion exchange mechanism was achieved for the preparation process, the morphology and particle size were not significantly affected but the calculated crystallinty index (CI) values were affected.

The absorption spectra of the doped samples are presented as absorption bands a typical $Mn^{+2,}$ and Fe^{+3} occupying to different crystalline sites. The obtained data agrees well with that obtained from XRD. The crystal field parameters and crystallinty index for sites of these ions in the HAp matrix were calculated. SEM analysis indicated that nanoparticles aggregates were formed. EPR properties make the studied sample to be used in the field of hyperthermia application.

Keywords: Hydroxyapatite, crystallinty index, nanoparticles and magnetic Hydroxyapatite

1. Introduction

UNDER PEER REVIEW

It well known that hydroxyapatite (HAp) is the main inorganic phase of human bones and teeth [1-3]. Hydroxyapatite (HA) is the main inorganic phase of human bones and teeth which consist of nearly 72 wt% apatitic materials for bone and 96 wt% for teeth. Calcium to phosphate ratio (Ca/P) in the building structure of HAp is 1.67. This ratio is very close to that Ca/P of natural bone [4-5]. Synthetic Hydroxyapatites have a wide range of applications both in medicine and dentistry due to its excellent bioactivity, osteoconductivity and biocompatibility [6-7]. The bioactivity behavior of HAps obtained from their ability to bond directly with the living tissues. The biocompatibility property comes from having no toxic effects on human tissues [8-9]. Hydroxyapatite (HAp) and other calcium phosphate (CaP) materials in addition to its excellent bioactive they have a good osteoconductive properties because of their similarity to natural bone material [10-11] . Implants coated with HAp promote a direct physiochemical bond with bone, which leads to more rapid implant fixation and the development of a stable bone biomaterial interface [12].

The main disadvantage of HAp is that they cannot be applicable to use for heavy load bearing applications due to its low mechanical properties in wet environments. The long term performance is limited by problems like coating adhesion, rapid dissolution, fatigue failure and the creation of particulate debris but in other way it has the ability to promote bone attachment [13].

Magnetic-nanoparticles are used in bio-applications are usually made from biocompatible materials such as magnetite (Fe_3O_4) for which susceptibility

UNDER PEER REVIEW

is large. These magnetic particles have to be integrates into structure of hydroxyapatite thus it has the potential to achieve localized tumor heating without any side effects i.e hyperthermia effects. One of the main biomedicine sciences is the hyperthermia application consists of targeting magnetic nanoparticles to tumor tissue followed by application of an external alternating magnetic field. The temperature in tumor tissue is increased to above 43°C, results in necrosis of cancer cells, then it does not damage surrounding normal tissue [14]. So, Magnetic hydroxyapatite is made by combining a super paramagnetic Fe_3O_4 nanoparticles and hydroxyapatite, thus it can form a composite material [15-16].

Nanoparticles are incorporated into different materials such as polymers, noble metals, metal oxides and silica. Many researchers have developed different magnetic nanoparticles of ferromagnetic bioglass ceramics which provide magnetic properties for hyperthermia purposes [17]. Many studies have indicated that HAp ceramics show no toxic effects, inflammatory response, and pyrogenetic response. It is well known that HAp ceramics have excellent fibrous tissue formation between implant and bone, then better ability to bond directly to the host bone [18].

It was reported that insertion of the spinel ferrite $MnFe_2O_4$ through a wet chemistry process resulted in nanoparticles having a core–shell structure (in which the core was made up of the ferrite and the shell of HAp. Synthetic HAp

UNDER PEER REVIEW

is capable of undergoing bonding osteogenesis and is relatively insoluble *in vivo* and successfully used in hard tissue surgery [19].

Mn^{2+} containing HAp and tri calcium phosphate (TCP) were studied previously [20-21]. The motivation for the addition of Mn^{2+} ions to HA was due to the fact that divalent Mn^{2+} has been linked to the activation of integrins which are defined as a family of receptors which mediate cellular interactions with extracellular matrix and cell surface ligands. In presence of Mn^{2+} ions, cell adhesion is promoted because the ligand affinity of integrin increases.

Copper (Cu) ions are of interest with respect to materials for bone regeneration because of their proangiogenic potential. The most important problems with synthetic bone scaffolds is fast decrease in cells' viability with increasing distance from the surface of the scaffold material, which occur from the inability of nutrients and oxygen to diffuse further than 150-200 μm from the surface without a blood supply [22]. Stimulating infiltration of blood vessels into a bone substitute scaffold could increase the viability of bone forming cells within the scaffold then hasten the healing process.

The aim of this study is to shed more lights on new categories of magnetic hydroxyapatites. These types are having a good degree of magnetic properties and compatibility properties. These types of hydroxyapatites contain Fe^{+3}, Mn^{+2}, Co^{+2} and Cu^{+2} ions into the structure of HAp aiming to limit formation of magnetic secondary phase and able to be manipulated in situ by magnetic forces. These new types of magnetic hydroxyapatites are good

UNDER PEER REVIEW

candidate to be used in hyperthermia applications. As a fact, the use of magnetic stimulation in the field of tumor treatment is one of the modern trends which have received increased attention in scientific circles.

2. Materials and Methods

2.1. Preparation hydroxyapatite with Ca/P molar ratio of 1.67

Analytical grades of calcium nitrate $Ca(NO_3)_2.4H_2O$ (Merck) and diammonium hydrogen Phosphate (NH4)2HPO4 (Sigma-Aldrich) with Ca/P molar ratio 1.67 were used to produce pure HA was produced using the following chemical reaction

$$\mathbf{10(Ca(NO_3)_2.4H_2O)+6((NH_4)_2.HPO_4)+8NH_4OH \rightarrow Ca_{10}(PO_4)_6.(OH)_2+20NH_4NO_3+46H_2O} \quad (1)$$

$MnCl_2.4H_2O$ (Sigma-Aldrich), $FeCl_3.6H_2O$ ((Merck)), $CoCl_2.6H_2O$ (Sigma-Aldrich), and $CuCl_2.2H_2O$ ((Merck), were used as sources of, Mn^{+2}, Fe^{+3} ,Co^{+2} and Cu^{+2} respectively [23]. The different types of hydroxyapatites were presented in table 1. To produce a pure hydroxyapatite sample, a calculated amount of calcium nitrate ($Ca(NO_3)_2.4H_2O$) was dissolved in 1L distilled water with vigorous stirring (2 h) to form 0.5 M/L. then, Calculated amount of diammonium hydrogen phosphate ($(NH_4)_2.HPO_4$) was also dissolved in 1L distilled water with vigorous stirring (2 h) to form 0.5 M/L and added drop wise to the calcium nitrate, the pH of the solution was adjusted to 10-11 using ammonia solution. The two solutions were mixed to obtain a Ca/P molar ration of 1.667 at a controlled constant pH of about 10-11. The mixture was

UNDER PEER REVIEW

continuously stirred about 1hr at temperature 80 ^{o}C, until a white transparent gel was obtained. The gel was cooled and incubating at 40 ^{o}C for 24 h until a white precipitate was produced. The precipitate was decanted and filtrated under vacuum by using sintered Buchner funnel with continued washing by distilled water to remove ammonia solution and then dried in oven at 90 ^{o}C. The powdered sample was sintered at 10 ^{o}C/min to 900 ^{o}C for 1 h then placed in air-cooling to ambient temperature. The sintered product was crushed using agate mortar and pestle to obtain resultant powder.

2.2. FTIR measurements

Fourier transform infrared absorption signals of the studied HAp samples were measured at room temperature (20 ^{o}C) in the wavelength range 4000-400 cm^{-1} using a computerized recording FTIR spectrometer (Mattson5000, USA). Fine powdered samples were mixed with KBr in the ratio 1:100 for quantitative analysis and the weighed mixtures were subjected to a load of 5t/cm^2 in an evocable i.e to produce clear homogenous discs. Then, the IR absorption spectra were immediately measured after preparing the discs to avoid moisture attack.

2.3. X-ray diffraction analysis

The structure of dried and calcined samples was assessed using an X-ray powder diffractometer (a Philips PW1390 X-ray diffractometer) with Cu Kα target (Ni filter), wavelength (λ) = 1.54 Å. C/S= 1 x 10^3, KV = 40, time constant (T.C) = 2 and mA = 25 was used. The Bragg's angle (2θ) in the range of 4–70°,

UNDER PEER REVIEW

step size = 0.02 and step time 0.4s at room temperature. Crystallographic identification of the phases of synthesized apatites was accomplished by comparing the experimental XRD patterns to standards complied by the Joint Committee on Powder Diffraction Standards (JCPDS).

The size of the crystallites responsible for the Bragg reflection of the (002) and (300) planes were determined using Scherer equation:

$$d = \frac{K\lambda}{\beta \cos \theta} \quad (2)$$

where d is the crystalline diameter in nm, β is the peak width at half-maximum peak height in radians, λ is the x-ray wavelength, typically 1.54 Å, and θ is the Bragg angle.

2.4. Electron paramagnetic resonance

Electron paramagnetic resonance (EPR) spectra were recorded at room temperature using a BRUKER ESP 300FT-EPR spectrometer.

2.5. Surface structural analysis using scanning electron microscopy

Scanning electron microscopic (SEM) investigations were performed on glass samples at room temperature using an SEM model Philips XL30 attached with energy dispersive X ray (EDX) unit, with accelerating voltage 30kV, magnification up to 400,000. Surfaces of studied samples were coated with gold for morphological investigations.

UNDER PEER REVIEW

3. Results and Discussion:

3.1 Interpretation of the FTIR spectra of the pure hydroxyapatite.

During preparation of hydroxyapatite, the gel formed during the precipitation is an amorphous calcium phosphate (non-crystalline). This gel is then dried and fired at temperature 900 ^{o}C which helps it to convert slowly to crystalline hydroxyapatite phase with Ca/P ratio 1.67 [24].

Fig. 1 show FTIR spectrum of pure HAp prepared by wet chemical method. All hydroxyapatite characteristic bands are shown clearly. The observed FTIR spectra of the studied different types of hydroxyapatites can be realized and interpreted as follows.

The asymmetric stretching (ν_3) and bending (ν_4) modes of PO_4^{-3} ions were detected at 1048, 605 and 565 cm^{-1}, respectively [25]. Symmetrical stretching modes of PO_4^{-3} ions ν_1 and ν_2 were also found at around 960 and 470 cm^{-1}, respectively [26]. Stretching mode of the hydroxyl group (OH^{-}) were detected at around 3570 and 1630 cm^{-1} respectively [27].

3.2 Measurement of crystallinty index using FTIR spectra of the pure hydroxyapatite

The splitting of the peak in the wavenumber range (500-700) cm^{-1} into a well-defined doublet indicates the presence of a fully crystalline solid [28]. This peak is attributed to antisymmetric bending of phosphate ions. This splitting of peak can be used to measure a crystallinty index (CI) of such prepared HAp [29]. With this index it can clearly show the effect of calcium ions substitution

UNDER PEER REVIEW

with other metal on the crystallinty of prepared material. A graphical representation shown in Fig. 2 for this method is to measure the splitting of phosphate ion antisymmetric bending mode at 600 cm^{-1}. The steps are summarized in the following section.

A base line was drawn at the bottom of the absorption band to mark the limit of (A_2) region of the band. The upper two edges of the splitted band connected to determine the region which limits what is called the splitting area (A_1). The relation between the two areas is defined to be as splitting function (SF) so, for an amorphous calcium phosphate a single broad peak exists; therefore the value of the splitting function also will be zero. The two areas A_1 and A_2 are calculated for the prepared HAp. Its values are 14.91 for A_1 and 28.78 for A_2. Then the calculated crystallinty index for pure HAp is 0.518±0.02.

A second method proposed by Weiner and Bar-Yosef [30]. In order to measure crystallinty index using FTIR, a baseline is drawn from 700 to 500 cm^{-1} and the heights of the bands ν_4 at 605 cm^{-1}, 565 cm^{-1} and 595 cm^{-1} are measured. The $(CI)_{FTIR}$ index is then the value calculated by the relation:

$$(CI)_{FTIR} = \frac{A_{565} + A_{605}}{A_{595}} \qquad (3)$$

This method is used to give an indication for the change in crystallization behavior. It can be seen from this equation that (CI) depends on the absorption values at the wavenumbers 605 cm^{-1}, 565 cm^{-1} and 595 cm^{-1} then the crystal size increases as the absorption at 565 and 605 cm^{-1} increase. CI decreases as

UNDER PEER REVIEW

the increase of absorption at 595 cm^{-1}. In a general case for a sample with a high concentration of non-crystalline phases, the $(CI)_{FTIR}$ index for a single peak in the range (700-500) cm^{-1} can be made by using $A_{565} \approx A_{605} \approx A_{595}$ (a sample with a high percentage of non-crystalline phase). The calculated value of $(CI)_{FTIR}$ in this case ≈ 2. In case of the presence of abundance of crystalline phases i.e a well-defined double peak, the values of absorbance at 565 $\approx$ 605 cm^{-1} and 595 be equal to 1/2, then $(CI)_{FTIR} \approx 4$. The calculated values of the crystallinty indices for the all prepared samples measured by the two methods are given in table 2.

3.3 Interpretation of the FTIR spectra of hydroxyapatite doped with Mn and Cu.

Fig. 3a shows FTIR of pure hydroxyapatite (HAp), Fig. 3b shows hydroxyapatite doped with Mn atoms at the expense of calcium atoms with the stoichiometric ratio of (Ca+metal)/P=1.667 and Fig. 3c hydroxyapatite doped with Mn and Cu atoms. The figure reveals some structural changes that may be attributed to conversion of crystalline structure hydroxyapatite to amorphous structure.

In Fig. 3c the peak in wavenumber range 500 to 700 cm^{-1} are now merged and becomes a broad peak rather than splitting in pure hydroxyapatite which is attributed to the presence of amorphous calcium phosphate. There is an increase in intensity of the peak at 720 cm^{-1} and the envelope in the ranges of 800 to 1300 cm^{-1} becomes broader, this may also attributed to amorphous structure.

UNDER PEER REVIEW

Sharpness of vibrational peaks at 972 cm^{-1}, 1160 cm^{-1} in hydroxyapatite decreases and the peaks become broader and less intense. The presence of small peak for C-O vibration bonds of carbonate group at 1423 cm^{-1} provided the information that this sample contained carbonate ion and the presence of the carbonate ions promoted the incorporation of cation in the doped apatite [31]. The stretching mode of the OH^- were detected at around 3570 and 1630 cm^{-1} respectively. Absence of the sharp vibrational peaks at 940cm^{-1}, 1110 cm^{-1} and 1178 cm^{-1} may also be seen. The presence of Cu-O species was confirmed by a band at 710-760 cm^{-1}, which was assigned to a Cu-O stretch (characteristic of Cu^{+2}) in O-Cu-O units [32]. The appearance of this feature was concurrent with greatly decreased intensity of the OH stretch (3572 cm^{-1}) and the OH liberation (631cm^{-1}) bands upon Cu doping. Bands related to OH stretches were disturbed by nearby Mn and Mn-Cu HAp and observed between 3100 and 3600 cm^{-1}. Additional bands of low intensities are visible at 818 cm^{-1} and 833 cm^{-1} .These bands can be assigned to v_1 and v_3 vibrations of MnO_4^{3-} groups.

3.4 Interpretation of the FTIR spectra of HAp, Fe-HAp and Fe-Co-HAp.

The observed characteristic broad peaks (Fig. 4b and 4c) representing the phosphate (PO_4^{3-}) group for the samples supported the formation of apatite. Additionally peaks for adsorbed water were also appeared in case of Fe-HAp sample. However due to sintering at 900^oC the broad peak of the PO_4^{3-}group significantly changed to sharp and distinct peaks as clear for sample

UNDER PEER REVIEW

Fe-HAp. Particularly, the significant gap between the band positions of PO_4^{3-} group at 560 cm^{-1} and 620 cm^{-1} suggested the formation of the HAp. This result was then subsequently confirmed from the XRD data. The width of the broad band in the range 1200-800 cm^{-1} increased in the sample Fe-Hap and

Clearly the characteristic band positions observed for both of the synthesized samples are in good agreement with that of pure HAp. This observation supported the formation of the expected cation substituted HAp within the present experimental protocol.

3.5 Interpretation of the XRD of the pure hydroxyapatite.

Fig. 5 shows XRD for pure HAp. All peaks are indexed to hexagonal lattice of $Ca_{10}(PO_4)_6.(OH)_2$ crystal. The wide and high peaks reveal that the pure HAp has a very small size (nano-particles), also excellent crystal quality and no impurities was detected by X-ray. The d spacing, intensities and lattice parameters for the Hexagonal HAp are compared with JCPDS Card (data file No. 74-0565) standard for HAp. The obtained lattice parameters are (a=9.424 and C=6.879) and the d values of the strongest three lines are 2.81, 2.72 and 2.78.

Person et al. [33] suggested a model that can be used to calculate crystallinty index using the X-ray powder diffraction patterns. In this model he suggested a several peaks that are very close to each other located in the 2θ range between 30 and 35° of a HAp X-ray chart. The reflections were (202),

UNDER PEER REVIEW

(300), (211), and (112). A baseline is drawn between 24 and 38° then the height of the highest peak with reflection (211) is measured from a baseline set between 24 and 38° of 2θ up to the top of the peak; $H_{(211)}$, and heights of the other peaks which are $H_{(202)}$, $H_{(300)}$ and $H_{(112)}$ measured from the top of the corresponding peak and the "valley" separating it from the next peak, this method can be represented as shown in Fig. 6 Then, the (CI) XRD value is calculated by the following relation mentioned in equation 4. All the X-ray spectra have been checked for the presence of other different magnetic atoms which are Mn, Cu, Fe and Co.

$$CI = \sum \frac{H_{(202)} + H_{(300)} + H_{(112)}}{H_{(211)}} \qquad \text{.....(4)}$$

3.6 Interpretation of the XRD of pure HAp, Mn-HAp and Mn-Cu-HAp

Fig. 7 shows XRD patterns of all samples HAp, Mn-HAp and Mn-Cu-HAp. In fig.7 (a) the peaks present agree well with ICSD file no. 74-0565 which is hexagonal hydroxyapatite and none of the patterns displayed extra peaks indicating that all samples were single phased HAp.

Fig. 7 (b,c) shows XRD for Mn ions substituted HAp and a combination between Mn and Cu ions. Compared with pure HAp, all metal ions substituted HAp in this case which are Mn and Cu ions, showed a comparable peaks without significant shifting of peak positions, regardless of substitution

UNDER PEER REVIEW

concentrations. This suggested that the ion exchange process did not greatly modify the structure of HAp.

The amount of manganese added distorted the structure unit of HAp and lower the degree of crystallinty to some extent and formation of a newly crystalline phases. These phases are manganese oxide (β-Mn_3O_4) ICSD file no. 86-2337, orthorhombic one with lattice parameters (a=9.55, b=9.79 and c=3.02) in cases of sample b in curve, and copper manganese oxide ($CuMn_2O_4$) ICSD file no. 45-0505 tetragonal phase with lattice parameters (a=5.971 and c=8.964) in cases of sample c in curve. Also, it can be noted that, lines corresponding to crystalline phases of other calcium-phosphate–based compounds are absent.

3.7 Interpretation of the XRD of pure HAp, Fe-HAp and Fe-Co-HAp

Fig. 8 shows XRD patterns of all samples HAp, Fe-HAp and Fe-Co-HAp. A similar behavior in XRD results for samples of Mn-HAp and Mn-Cu-HAp. The peak positions are not clearly changed, but the peaks intensity changed and thus the degree of crystallization gradually. Clearly a number of prominent peaks for apatite phase were in the XRD pattern. However, the observed intensity and d-spacing values for both the samples are in excellent agreement with the JCPDS standard data for HAp.

The amount of Fe added to the basic hydroxyapatite changes the basic structural unit and lowers the degree of crystallinty by formation of newly crystalline phases. These phases are magnetite (Fe_3O_4) iron oxide, ICSD file no.

UNDER PEER REVIEW

89-0951, cubic with lattice parameters (a=8.491) in cases of sample b in curve, and cobalt iron oxide or cobalt ferrite ($CoFe_2O_4$) ICSD file no. 22-1086 cubic phase with lattice parameters (a=8.391) in cases of sample c in curve. Also, it can be noted that, lines corresponding to crystalline phases of other calcium-phosphate–based compounds are absent.

The XRD spectrum (Figure 3b) of the Mn-doped apatite shows the presence of amorphous phase which supports the observed FTIR data. The reason of this nature is the temperature effect. It is well established that the degree of crystallinty increases with the increase of sintering temperature resulting several distinct peaks.

Analysis an increase of the a axis and a decrease of c axis was detected as expected in the case of Ca substitution with ion species having a lower radius. This observation confirmed the formation of Fe-HAp, Mn-HAp, Fe-Co-HAp and Mn-Cu-HAp substituted apatite of hexagonal structure and conclusively proved that a variety of substitutions of both cationic and anionic is possible in hydroxyapatite structure without any significant modification of its hexagonal system.

The crystallite size, crystallinty index and lattice parameters of doped and calcined (at 900°C) samples were calculated as described previously. The calculated values are tabulated in Table 2.

UNDER PEER REVIEW

The lattice parameters and cell volume values of the Fe-HAp did not significantly change as compared to those of pure HA. But in case of Fe-Co- HAp doped apatite, lattice parameters values are lower than that observed in case of pure HAp.

However for both cases lower values of crystallite size and crystallinty were observed as substitution significantly reduces the crystallite size as well as crystallinty. Possibly, the changes in cell volume for the latter case would be due to the substitution of more cation. The crystallinty indices were measured by FTIR and XRD are written in table 3.

3.8 SEM and EDX analysis

Fig. 9 shows a scanning electron microscope (SEM) and energy dispersive x-ray analysis (EDX) for different samples. As clear from the SEM micrographs, the thin-film surface morphology is characterized by a granular structure, composed of grains that are tens of nanometers in size. The micrographs showed hydroxyapatite (HAp) was present in most of the areas of each studied sample. Since the synthesized hydroxyapatites showed the presence of crystalline phase after sintering at 900 ^{o}C. So the morphology and micro structural nature of the metal substituted apatites synthesized at this temperature were observed by SEM. The presence of Mn, Cu, Fe and Co in structure of hydroxyapatites was confirmed by EDX. Furthermore, the roughness of the surfaces may be enhanced by the presence of spherical particulates with dimensions in the micrometer range. Rough surfaces do not

UNDER PEER REVIEW

present a problem for biocompatible of implants since it was found that surfaces with certain roughness ensure a better osteointegration as compared to smooth implants [34].

3.9 Interpretation of EPR for HAp, Fe-Co-HAp and Mn-Cu-HAp

It well known that the total magnetic field of each ion is established from the spin-spin interaction of neighboring paramagnetic ions [35]. The spin-spin interaction caused by small magnetic fields and this play an important role to alter the total magnetic field of each ion. So, the energy levels of the unpaired electrons to be shifted which led to a variation of energies resulting in a broadened EPR signal.

In Fe-HAp sample (as shown in Fig. 10), the broad feature in the g of 2.0 region is attributed to separation of ferric oxide phases with different content in iron cations (Fe^{2+} and Fe^{3+}), and their separation results presence of surface oxyhydroxides and Fe-O-Fe clusters [36]. The presence of high concentration of Fe^{3} caused electron spin-spin interactions between neighboring Fe^{+3} nuclei which yielded the broad g 2.0 signal. The poor crystallinty with sample Fe-HAp that results from the Fe-phosphates and Fe-oxyhydroxides would be expected to have a high concentration of neighboring Fe^{3} ions. These agree well with results of XRD and FTIR results. The rhombic crystal field symmetry assigned to Fe-SHA suggested that Fe^{3} was occupying the rhombic Ca(2) site, and not the axial Ca(1) site. However, charge compensation from Fe^{+3} substituting for Ca^{+2} could cause a symmetry distortion and lead to a rhombic environment in the Ca(1)

UNDER PEER REVIEW

363 site.

364 The number and position of EPR transitions for isolated Fe^{3+} ions in a site
365 of well-defined symmetry observable in a powder spectrum depends sensitively
366 on the local ligand-field symmetry of the sites and possible magnetic
367 interactions between them. In the presence of a rhombic distortion of the ligand-
368 field the g values of the three doublets of the S = 5/2 system change as a zero-
369 field splitting parameters depending of its value it becomes possible to observe
370 ESR signal arising from the ± 3/2 and ± 5/2 doublet of the excited states. Iron
371 (III) rhombic crystal field symmetry may indicate substitution into either of the
372 Ca sites in Fe-HAp.

373 The Fe-Co-HAp had lower g-value 2.0 peak intensity relative to the g-
374 value 2.0 peak intensity of Fe-HAp. This suggests that nonstructural poorly
375 crystalline Fe-oxyhydroxides or Fe-phosphates phases were associated with the
376 HAp crystallites [37].

377 Manganese (IV) may be the cause of the low field X-band hyperfine
378 patterns. Manganese (IV) would have originated from Mn^{+2} oxidation during
379 Mn-HAp synthesis. However, the pink color of the Mn-SHA materials indicated
380 that Mn^{+2} was the dominant oxidation state in the g-value 2 [38].

381 The hyperfine lines of the Mn-Cu-HAp were barely detectable. Minor
382 spectral differences were observed between the Mn-Cu-HAp and Fe-Co-HAp
383 showed a marked decrease in peak intensity relative to standard HAp.

384 The large decrease of the Mn-Cu-HAp g 2.01 peak indicated that

UNDER PEER REVIEW

nonstructural Mn phase(s) such as poorly crystalline Mn-oxyhydroxide and Mn-phosphate phase(s) associated with the SHA crystallites [39]. Poorly crystalline Mn phase(s) also explain the broad g-value 2.01 peak in Mn-HAp that was superimposed on the hyperfine pattern because Mn^{+2} would be closely associated with one another leading to spin-spin interactions.

The central sharp peak observed in Mn-HAp and was possibly from a small concentration of an inorganic or organic contaminant in the synthesis reagents. The high intensity of the Mn^{+2} peaks Mn-HAp dominated the spectrum and masked any contamination peak.

Spin-spin exchange interactions because of Mn and Cu atoms were cause of an increase of signal broadening [40]. The entire Fe-Co-HAp spectrum was superimposed on the broad signal that suggested the presence of sites with strong spin-spin interactions caused by poorly crystalline Fe-oxyhydroxide or Fe-phosphate phase(s).

4. Conclusion:

Nano-sized particles of pure HAp and various Fe, Mn, Fe-Co and Mn-Cu doped HAp powders have been successfully prepared via a novel wet chemical method. Doping of Fe into HAp powders has greatly influenced the crystallinty in a trend that the crystallinty were decreased with Fe substitution. A similar behavior was obtained for Mn. Addition of Co to sample Fe-HAp greatly decreases the crystallinty index. Also, addition of Cu to Mn-HAp was found to do the same effect. This is in good agreement with the FTIR result where the

UNDER PEER REVIEW

splitting of band in wavenumber range 500-700 cm^{-1} is decreased up on addition of different metal ions in substitution of Ca. The data obtained from XRD for different powder samples were found to be in a good agreement with that obtained from FTIR. The crystallinty index was found to decrease upon substitution and the intensities of lines were also decreased. Our results indicate that nano-crystallites of the Co-ferrite ($CoFe_2O_4$) and magnetite (Fe_3O_4) are being formed in a hydroxyapatite. When a further investigation will be carried out using SEM, EDX and EPR, it was found the magnetic properties they have will play a vital role to enhance the bioactivity and physiochemical properties of the apatite.

5. References

[1] Nudelman F., Pieterse K., George A.: Nature materials 9, 1004-1009 (2010).

[2] Zhou H., Lee J.: Acta Biomaterialia 7, 2769-2781 (2011).

[3] Swetha M., Sahithi K., Moorthi A.: International journal of biological macromolecules 47, 1-4 (2010).

[4] LeGeros R. Z., Ito A., Ishikawa K.: Advanced Biomaterials: Fundamentals, Processing, and Applications 19-52 (2010).

[5] Gergely G., Wéber F., Lukács I.: Ceramics International 36, 803-806 (2010).

[6] Uskoković V., Uskoković D. P.: Journal of Biomedical Materials Research Part B: Applied Biomaterials 96, 152-191 (2011).

[7] Sadat-Shojai M., Atai M., Nodehi A.: dental materials 26, 471-482 (2010).

UNDER PEER REVIEW

[8] Li M., Wang Y., Liu Q.: Journal of Materials Chemistry B 1, 475-484 (2013).

[9] Chen Y., Huang Z., Li X.: Journal of Nanomaterials 2012, 3 (2012).

[10] Cheng L., Ye F., Yang R.: Acta biomaterialia 6, 1569-1574 (2010).

[11] Ripamonti U., Roden L. C., Renton L. F.: Biomaterials 33, 3813-3823 (2012).

[12] Maxian S. H., Zawadsky J. P., Dunn M. G.: Journal of biomedical materials research 27, 111-117 (1993).

[13] Kane R. J., Roeder R. K.: Journal of the mechanical behavior of biomedical materials 7, 41-49 (2012).

[14] Neuwelt E. A., Várallyay C. G., Manninger S.: Neurosurgery 60, 601-612 (2007).

[15] Reddy L. H., Arias J. L., Nicolas J.: Chemical reviews 112, 5818-5878 (2012).

[16] Ge F., Li M.-M., Ye H.: Journal of hazardous materials 211, 366-372 (2012).

[17] Lu A. H., Salabas E. e. L., Schüth F.: Angewandte Chemie International Edition 46, 1222-1244 (2007).

[18] Pankhurst Q. A., Connolly J., Jones S.: Journal of physics D: Applied physics 36, R167 (2003).

[19] Wei G., Ma P. X.: Biomaterials 25, 4749-4757 (2004).

UNDER PEER REVIEW

449 [20] Pereira Moreira M., Teixeira da Silva Aragão V., de Almeida Soares G. D.:
450 Key Engineering Materials 493, 20-26 (2012).
451 [21] Mayer I., Cohen S., Gdalya S.: Materials Research Bulletin 43, 447-452
452 (2008).
453 [22] Barralet J., Gbureck U., Habibovic P.: Tissue Engineering Part A 15, 1601-
454 1609 (2009).
455 [23] El-Bahy G., Abdelrazek E., Hezma A.: Journal of Applied Polymer
456 Science 122, 3270-3276 (2011).
457 [24] Shadanbaz S., Dias G. J.: Acta biomaterialia 8, 20-30 (2012).
458 [25] Chang C., Peng N., He M.: Carbohydrate polymers 91, 7-13 (2013).
459 [26] Shen Y., Liu J., Lin K.: Materials Letters 70, 76-79 (2012).
460 [27] Rehman I., Bonfield W.: Journal of Materials Science: Materials in
461 Medicine 8, 1-4 (1997).
462 [28] Termine J. D., Posner A. S.: Nature 211, 268-270 (1966).
463 [29] Farlay D., Panczer G., Rey C.: Journal of bone and mineral metabolism 28,
464 433-445 (2010).
465 [30] Weiner S., Bar-Yosef O., Stiner M. C.: Journal of Archaeological Science
466 22, 223-237 (1995).
467 [31] Paluszkiewicz C., Ślósarczyk A., Pijocha D.: Journal of Molecular
468 Structure 976, 301-309 (2010).
469 [32] Stanić V., Dimitrijević S., Antić-Stanković J.: Applied Surface Science
470 256, 6083-6089 (2010).

UNDER PEER REVIEW

[33] Person A., Bocherens H., Salie`ge J.-F.: Journal of Archaeological Science 22, 211–221 (1995).

[34] Brunette, Maxwell D.: Titanium in medicine: material science, surface science, engineering, biological responses, and medical applications, ed., Springer, 2001.

[35] Desrosiers M., Schauer D. A.: Nuclear Instruments and Methods in Physics Research Section B: beam interactions with materials and atoms 184, 219-228 (2001).

[36] Jiang M., Terra J., Rossi A.: Physical Review B 66, 224107 (2002).

[37] McAlpin J. G., Stich T. A., Casey W.: Coordination Chemistry Reviews 256, 2445-2452 (2012).

[38] Oliveira L., Rossi A., Baffa O.: Applied Radiation and Isotopes 70, 533-537 (2012).

[39] Ravindranadh K., Babu B., Manjari V. P.: Journal of Luminescence (2014).

[40] Chaikina M., Bulina N., Ishchenko A.: Russian Physics Journal 56, 1176-1182 (2014).

6. Figure Captions

Fig.1 FTIR of pure hydroxyapatite (HAp).

Fig.2 A sketch represents position of areas A_1 and A_2 used to calculate the crystallinty index also absorptions at wavenumbers 565,595 and 605 cm^{-1} also illustrated.

UNDER PEER REVIEW

Fig.3 FTIR of (a) pure hydroxyapatite HAp,(b) Mn-HAp and (C) Mn-Cu-HAp

Fig.4 FTIR of (a) pure hydroxyapatite HAp,(b) Fe-HAp and (C) Fe-Co-HAp

Fig.5 XRD of pure HAp.

Fig.6 Person's Model for measuring crystallinty indices for hydroxyapatites. The represented spectrum is for pure HAp (2θ from 25 to 40).

Fig.7 XRD of pure hydroxyapatite and HAp, Mn-HAp and Mn-Cu-HAp.

Fig.8 XRD of pure hydroxyapatite and HAp, Fe-HAp and Fe-Co-HAp.

Fig.9 SEM and EDX of(a) pure hydroxyapatite HAp, (b)Fe-Co-HAp.

Fig.10 EPR of pure HAp, Fe-Co-HAp and Mn-Cu-HAp.

7. Tables Captions

Table 1 Chemical formulas and symbols for prepared samples.

Table 2 Crystallite size, degree of crystallinty and lattice parameters for prepared powder samples

UNDER PEER REVIEW

Table 3 $(CI)_{FTIR(areas)}$ measured by areas method , $(CI)_{FTIR(height)}$ measured by height method and $(CI)_{XRD}$ for prepared powder samples

490

Chemical Formula	Symbol
$Ca_{10}(PO_4)_6.(OH)_2$	HAp
$Ca_{7.6}Mn_{2.4}(PO_4)_6(OH)_2$	Mn- HAp
$Ca_{7.6}Mn_{1.6}Cu_{0.8}(PO_4)_6(OH)_2$	Mn-Cu-HAp
$Ca_{7.6}Fe_{2.4}(PO_4)_6(OH)_2$	Fe- HAp
$Ca_{7.6}Fe_{1.6}Co_{0.8}(PO_4)_6(OH)_2$	Fe-Co- HAp

491 *Table (1)*

492

Symbol	Crystallite size	Degree of crystallinty	Lattice parameters	
HAp	28.76 nm	81.3%	a=9.420Å	c=6.881 Å
Mn-HAp	28.90 nm	59.2%	a=9.592 Å	c=6.870 Å
Mn-Cu-HAp	29.01 nm	43.6%	a=9.454 Å	c=6.869 Å
Fe-HAp	28.63 nm	61.8%	a=9.451 Å	c=6.873 Å
Fe-Co-HAp	29.05 nm	41.3%	a=9.450 Å	c=6.872 Å

493 *Table (2)*

Symbol	$(CI)_{FTIR(areas)}$	$(CI)_{FTIR(heights)}$	$(CI)_{XRD}$
HAp	0.518	2.36	0.376
Mn-Hap	0.467	2.11	0.315

UNDER PEER REVIEW

Mn-Cu-HAp	0.413	1.87	0.246
Fe-HAp	0.483	2.21	0.327
Fe-Co-HAp	0.238	1.08	0.264

494 *Table (3)*

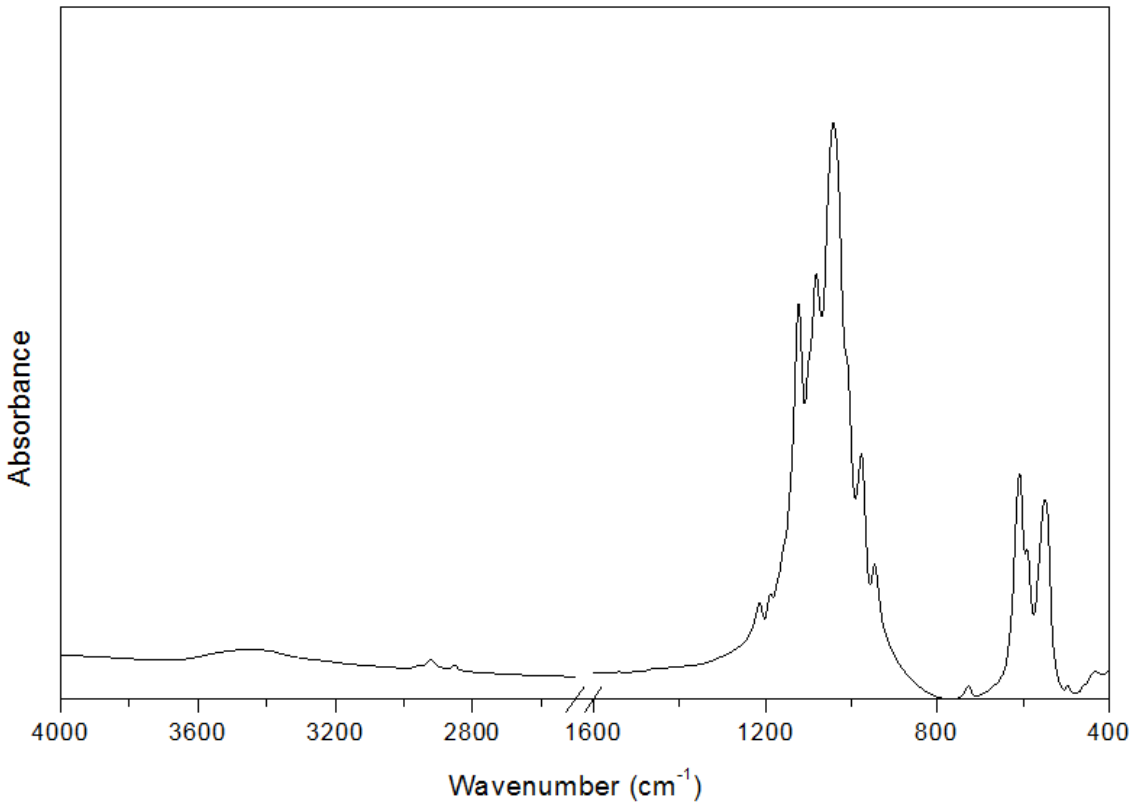

495

496 Fig.1

UNDER PEER REVIEW

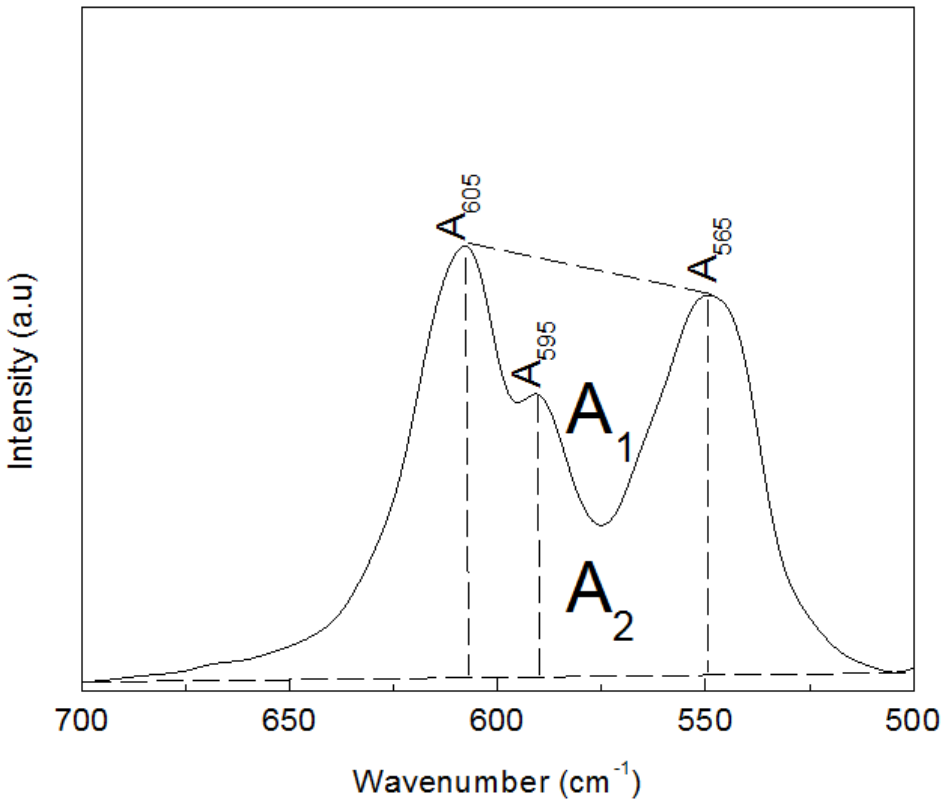

497

498 Fig.2

UNDER PEER REVIEW

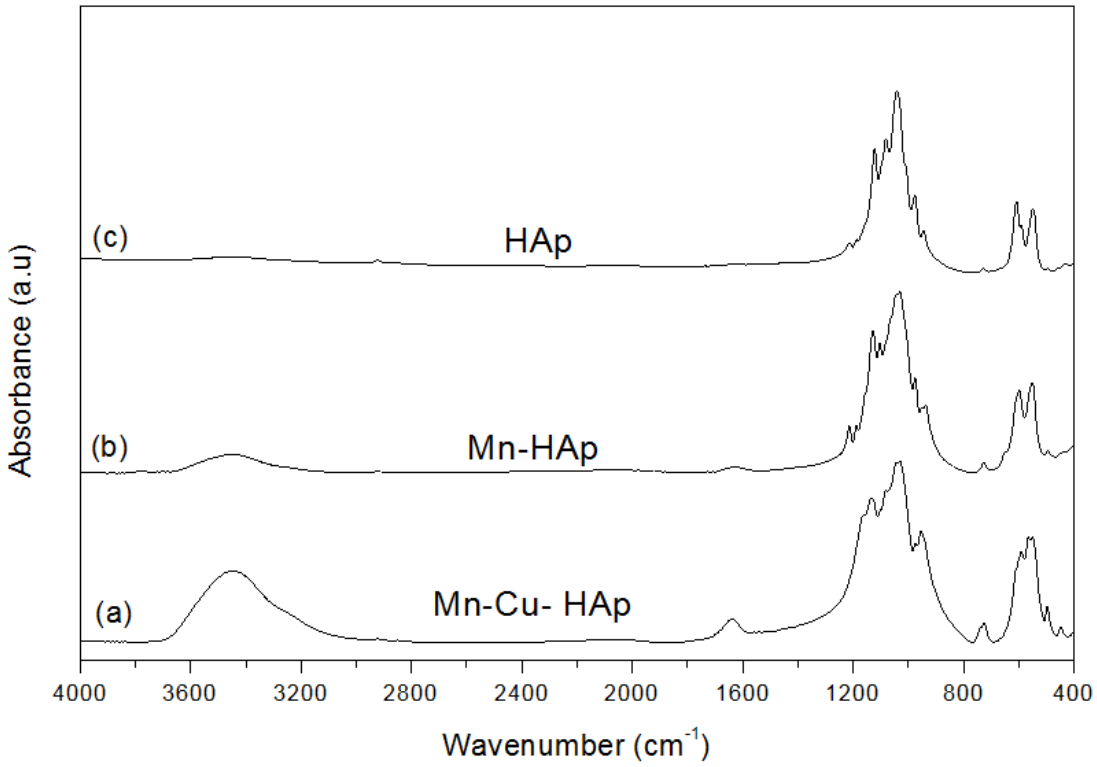

499

500 Fig.3

UNDER PEER REVIEW

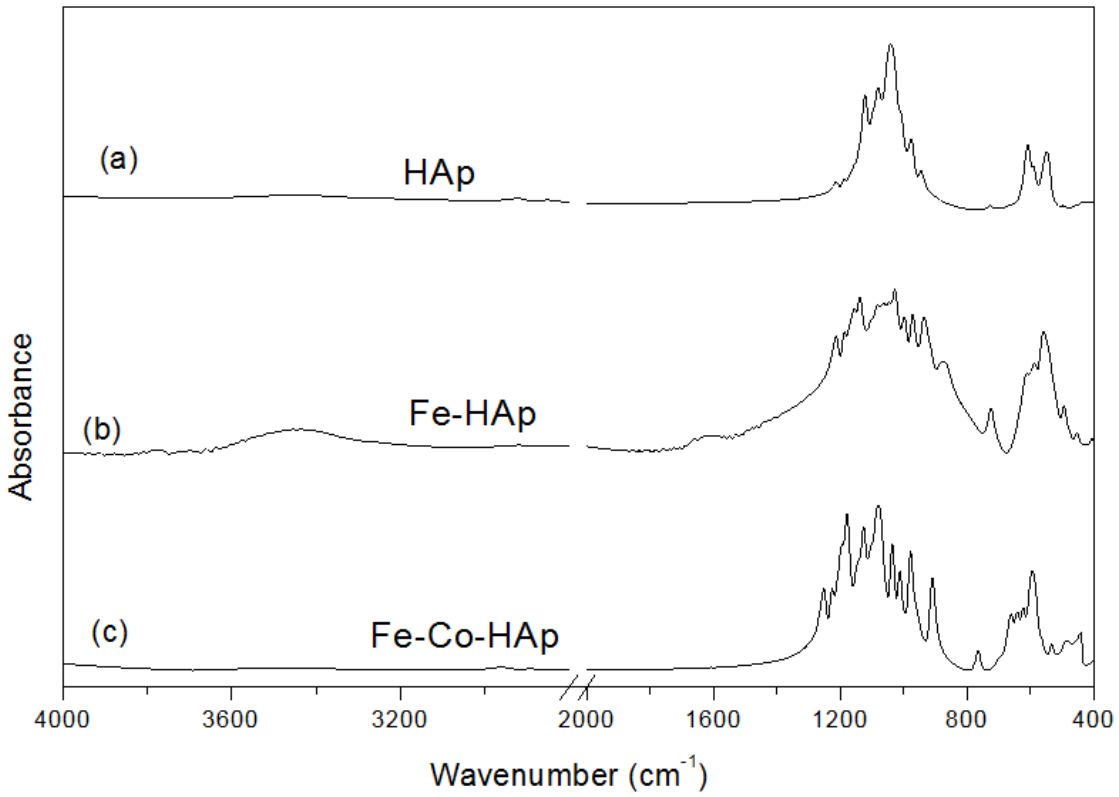

501

502 Fig.4

UNDER PEER REVIEW

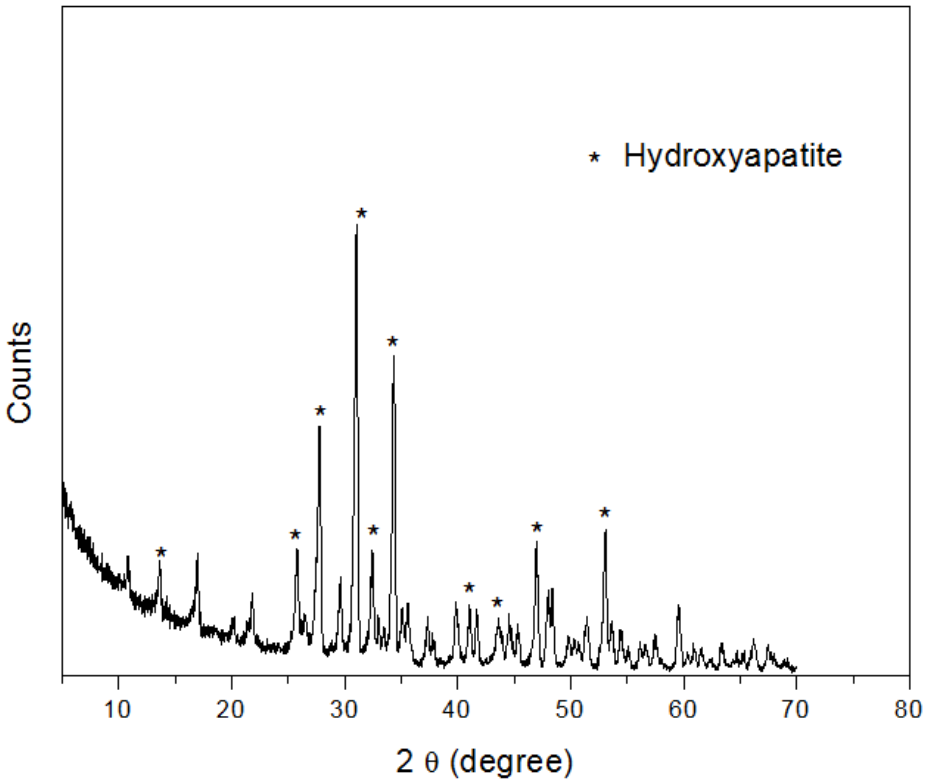

503

504 Fig.5

505

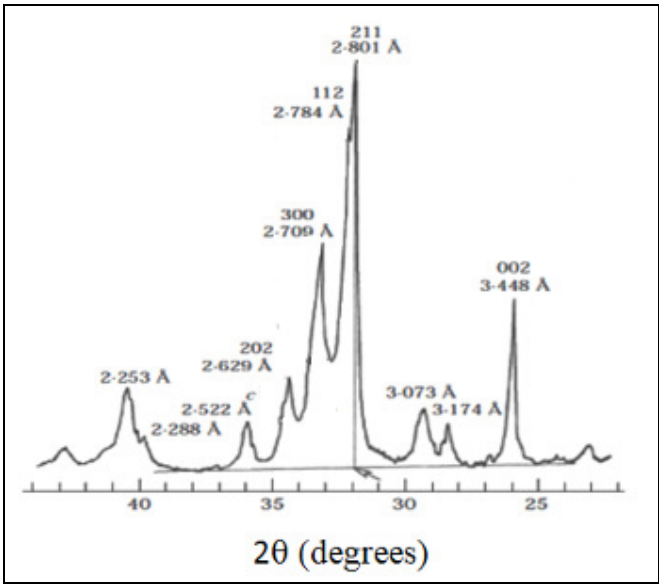

506

507 Fig.6

UNDER PEER REVIEW

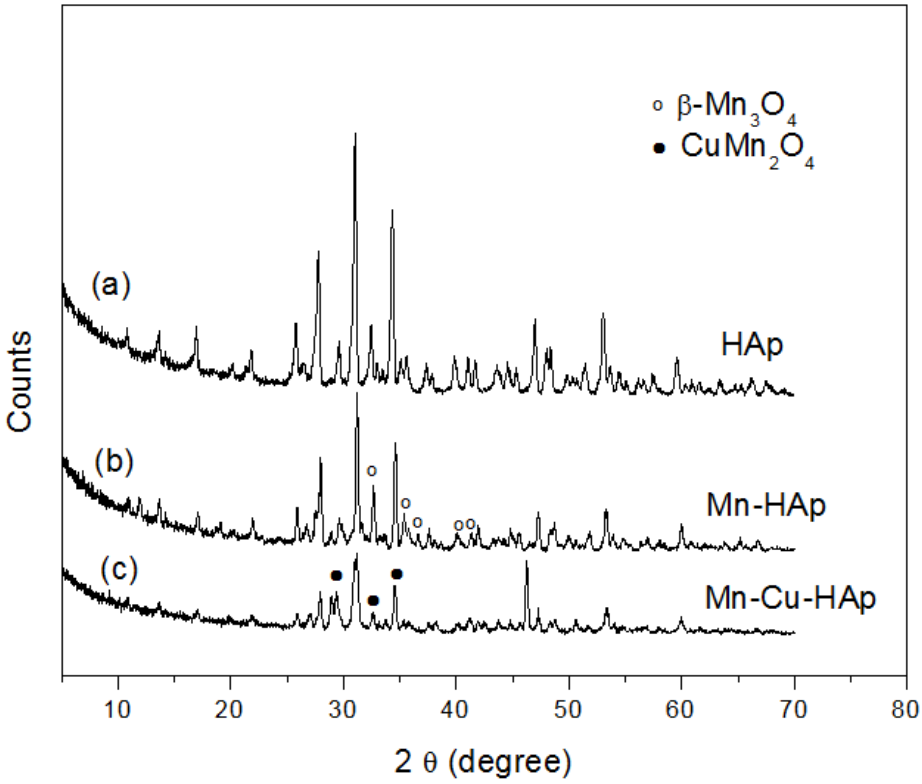

508

509 Fig.7

510

511

512

513

514

515

516

517

518

UNDER PEER REVIEW

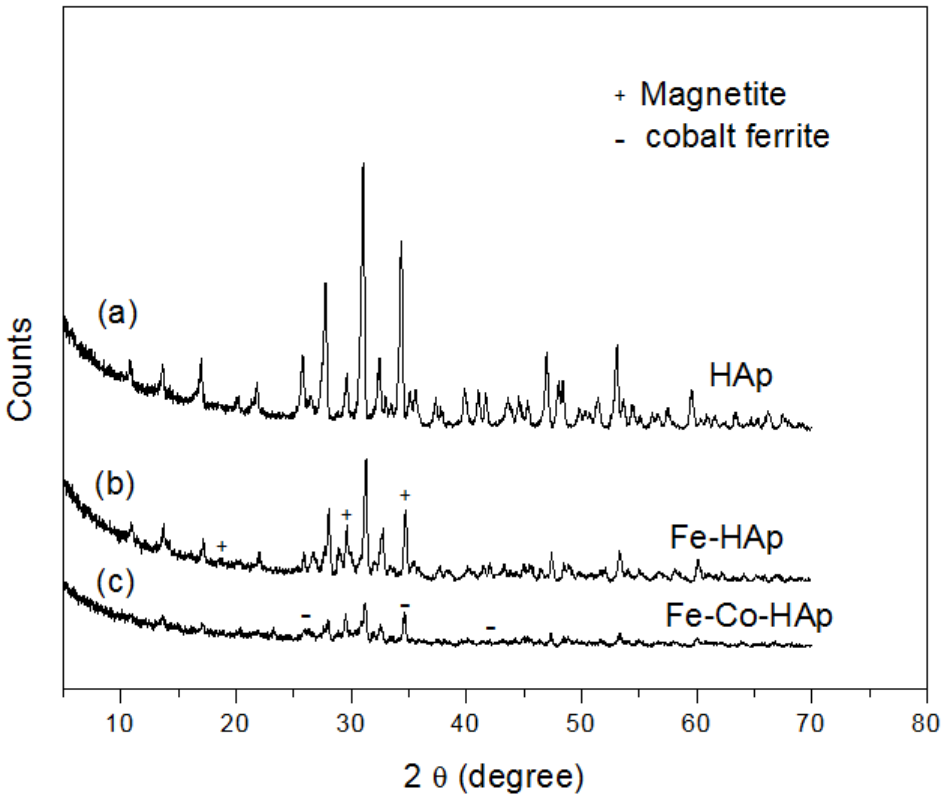

519

520 Fig.8

UNDER PEER REVIEW

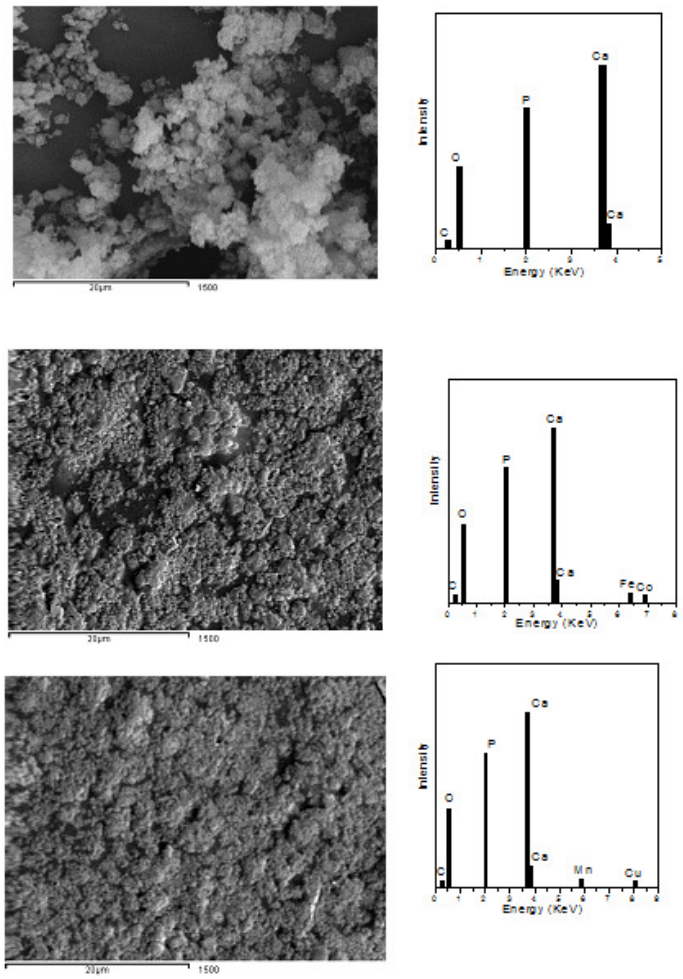

521

522 Fig.9

UNDER PEER REVIEW

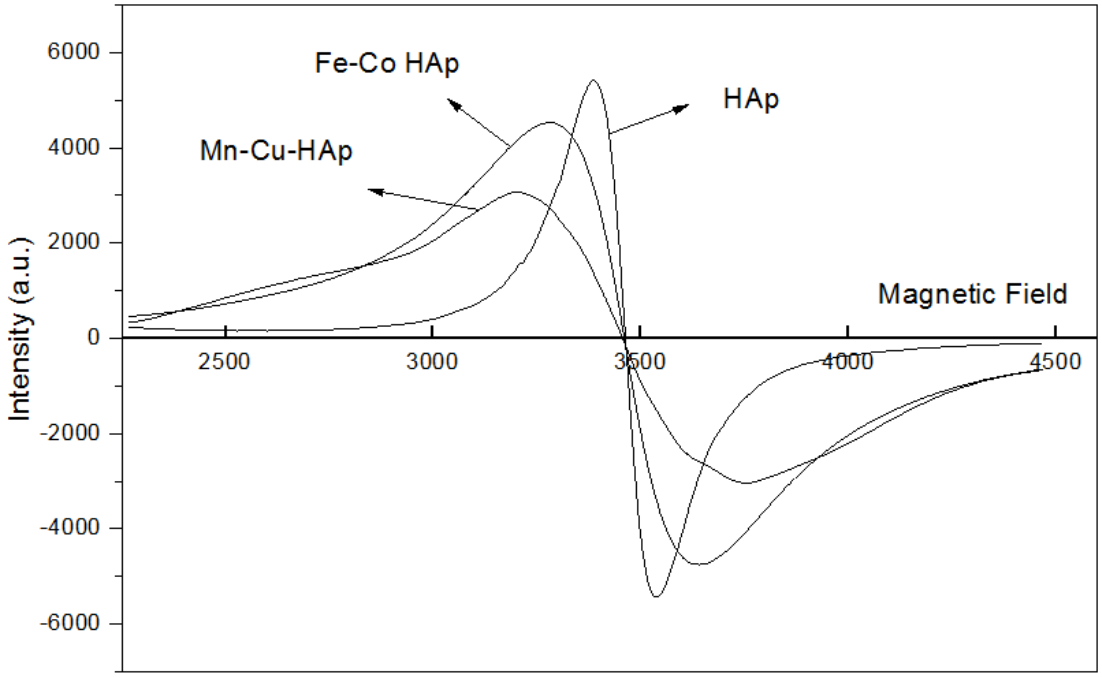

523

524 Fig.10